A Reflectionless Receiver With Absorptive IF Amplifier and Dual-Path Noise-Canceling LNA

Zhixian Deng, *Graduate Student Member, IEEE*, Huizhen Jenny Qian, *Member, IEEE*, and Xun Luo, *Senior Member, IEEE*

***Abstract*— This article presents a 22.6–39.2-GHz reflectionless receiver (RX) capable of reducing the in-band intermodulation and high-order mixing products. Such RX consists of an absorptive IF amplifier, a double-balance passive mixer, and a dual-path noise-canceling low noise amplifier (LNA). The absorptive IF amplifier is utilized to suppress the out-of-band signal reflected back to mixer, which can reduce the intermodulation and high-order mixing products caused by the remixing of the out-of-band signals. Meanwhile, the dual-path noise-canceling LNA is used for achieving low noise figure (NF) in a wide frequency range. To verify the aforementioned principle, a reflectionless RX is implemented and fabricated using a conventional 28-nm CMOS technology. The measurement shows the minimum NF of 3.6 dB and the peak input third-order intercept point (IIP3) of −11.7 dBm. Besides, the proposed RX can support multi-Gb/s, 256-quadratic amplitude modulation (QAM)/1024-QAM modulation signals.**

***Index Terms*— Absorptive IF amplifier, CMOS, high-order mixing product, receiver (RX), reflectionless.**

I. Introduction

MODERN multi-standard wireless systems provide high data rates using the wideband millimeter-wave spectrum and high-order modulation. As the key sub-system in the wideband wireless systems, the receiver (RX) should be developed with high dynamic range and high signal quality within a wide operating frequency range. Therefore, multiple technologies, such as linearity improvement [1], [2] and noise canceling [3], [4], are developed and introduced to the wideband RX with sub-circuit designs. However, the ever-developing of modern and coming wireless applications (e.g., 5G, vehicles, and intelligent manufacturing) occupies the spectrum and makes the wideband RX operate in a complicated electromagnetic (EM) environment, where multiple in-band RF signals (i.e., desired signal, imaging signals, and blockers) are received by the RX in practical applications. Meanwhile, the receiving signals along with the local oscillator (LO) signal generate unpredictable intermodulation and high-order mixing products in the non-linear device of RX. Those imaging signals, blockers, and mixing products located in the receiving channel (i.e., RF domain and IF domain) interfere with the desired signals, hence degenerating the RX performance significantly. The image signal can be located at the stopband of the RF domain and suppressed by an RF filter once the high IF architecture is used [5]. Besides, the image signal allocated in RF passband can be reduced using the IQ architecture [6]–[11]. For the in-band blocker suppression, the spatial filter can be utilized in the RX array systems [12]–[17].

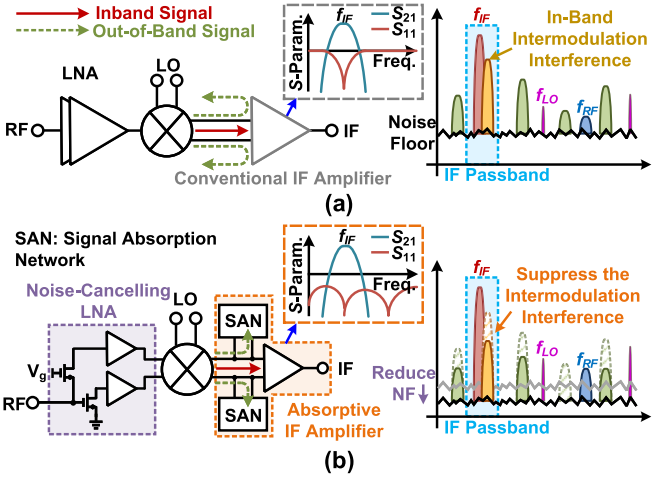

Fig. 1. Principle and configuration of (a) conventional heterodyne RX and (b) proposed reflectionless RX with absorptive amplifier and dual-path noise-canceling LNA.

The recent studies reveal that the intermodulation can be suppressed by reducing the inter-stage signal reflection between mixer and filter in the RX systems [18], [19]. The key to achieve such non-reflection operation is utilizing the absorptive or reflectionless components in the IF domain. Conventional absorptive or reflectionless components are mainly designed in two topologies.

1) Introducing a symmetrical network to ensure that the even- and odd-mode reflection coefficients of the two-port components are equal in amplitude and opposite in sign (i.e., $\Gamma_e = -\Gamma_o$), therefore, the reflection of the two-port components can be theoretically reduced to zero in a wide frequency range [20].
2) Design an auxiliary signal path with the complementary frequency response to the main signal path (e.g., bandstop auxiliary path to the bandpass main path, both

Manuscript received 16 August 2021; revised 19 November 2021 and 16 January 2022; accepted 18 January 2022. Date of publication 10 February 2022; date of current version 25 July 2022. This article was approved by Associate Editor Pietro Andreani. This work was supported in part by the National Natural Science Foundation of China under Grant 61934001, Grant 62174020, and Grant 62161160310. *(Corresponding author: Xun Luo.)*

The authors are with the Center for Advanced Semiconductor and Integrated Micro-System, University of Electronic Science and Technology of China, Chengdu 611731, China (e-mail: xun-luo@ieee.org).

Color versions of one or more figures in this article are available at https://doi.org/10.1109/JSSC.2022.3145054.

Digital Object Identifier 10.1109/JSSC.2022.3145054

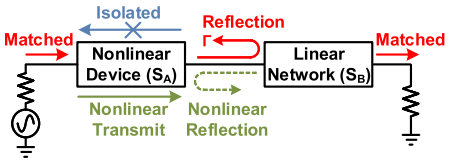

Fig. 2. Configuration of a nonlinear device connected with a linear network.

operated at the same center frequency with the same bandwidth), where the out-of-band signal is dissipated in the loaded resistor of auxiliary path [21].

Nonetheless, the aforementioned two topologies require one or multiple 1/4 wavelength transmission lines that limit the application in a compact integrated RX design. Therefore, using a reflectionless technique to suppress the intermodulation in high-performance integrated RX still remains a great challenge.

This article is an extension of the authors' previous work [22], which presents a reflectionless RX capable of reducing the in-band intermodulation interference and high-order mixing products. Such RX consists of an absorptive IF amplifier, a double-balance mixer, and a dual-path noise-canceling low noise amplifier (LNA). Then, the proposed reflectionless RX is designed and implemented in a 28-nm CMOS technology for verification, while the measured result exhibits a state-of-the-art performance. This article is organized as follows. The prototypes with principle and theoretical analysis of the reflectionless RX and absorptive IF amplifier is discussed in Section II, while Section III presents the circuit implementation. In Section IV, the proposed reflectionless RX is fabricated, measured, and compared with the state of the arts. The conclusion is summarized in Section V.

II. Principle and Operation

Fig. 1(a) shows the typical configuration of a heterodyne RX [23], [24]. After amplifying by the LNA, the RF signal is mixing with the LO in the nonlinear mixer, hence generating the mixing products, including the required IF signal, harmonics, and intermodulation. In general, the IF domain of such RX consists of the IF amplifier and IF filter with bandpass filtering function, which can increase the IF signal gain and prevent the unwanted mixing products from interfering in the following stages. The conventional IF filter with bandpass response reflects the out-of-band signals back to the mixer, and those reflected signals will generate additional undesired intermodulation and high-order mixing products by remixing with the RF and LO signals. Most of the unwanted signals can be reduced by the IF filter. However, the increasingly complex EM environments in modern wireless systems make the mixing products unpredictable. In some cases, some of the mixing products that fall into the IF passband cannot be suppressed by the IF filter, which will interfere with the IF signal and influence the RX performance significantly. Therefore, the reflcetionless operation can be introduced into the RX to reduce the interference caused by the signal reflection.

The architecture of the proposed reflectionless RX is shown in Fig. 1(b), which consists of a noise-canceling LNA,

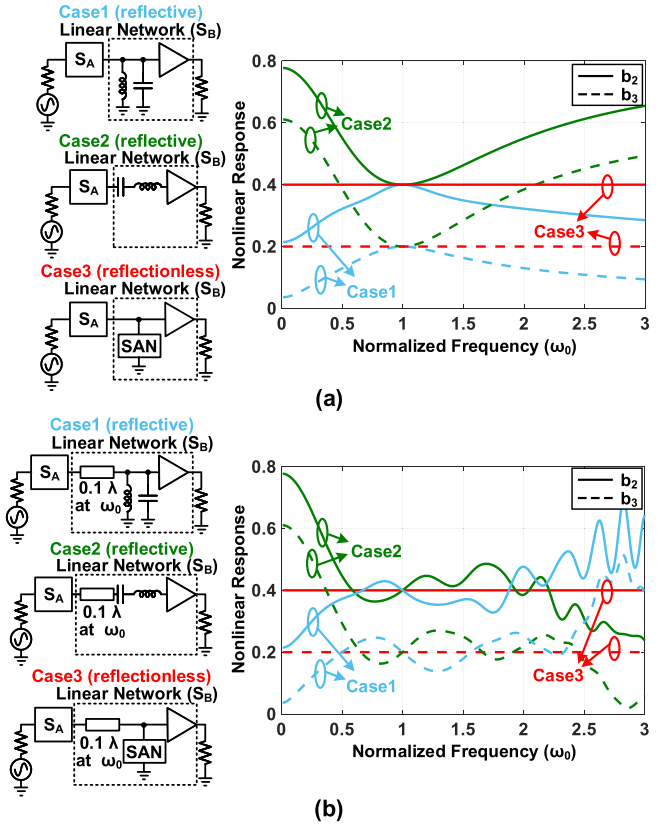

Fig. 3. (a) Calculated nonlinear response in different cases without interconnection. (b) Calculated nonlinear response in different cases with interconnection. Nonlinear parameters $n_{t12} = n_{t21} = 0.4$, $n_{t13} = n_{t31} = 0.2$, $n_{t23} = n_{t32} = 0.1$, and $n_{r12} = n_{r21} = n_{r13} = n_{r31} = n_{r23} = n_{r32} = 0.2$ are used for calculation, while the inductance, capacitance, and resistance are normalized.

a double-balance mixer, and a differential absorptive IF amplifier. Compared to the conventional RX, the absorptive IF amplifier is utilized to replace the reflect-type IF circuit. Such an absorptive IF amplifier can provide a bandpass response, while the signal absorption networks are used to dissipate the out-of-band signals without reflecting them back to the mixer. Therefore, the high-order mixing products and intermodulation interference caused by the remixing of the reflected signal can be suppressed, and the received signal quality can be improved. Meanwhile, the double-balance mixer is utilized to suppress the LO leakage. Besides, the noise-canceling LNA is introduced to reduce the noise figure (NF), hence improving the signal-to-noise ratio (SNR). To further clarify the aforementioned mechanisms, the rest of this section will provide the detailed analysis of the principle and sub-circuit design of the proposed reflectionless RX.

A. Linearity Enhancement Using Reflectionless Operation

In the RX system, the high-order mixing products and intermodulation interference are induced due to the nonlinearity of active devices, especially the mixer. In general, the mixer generates high-order mixing products not only from the RF and LO signals but also from the reflection signals of IF amplifier. To analyze the effect of signal reflection between

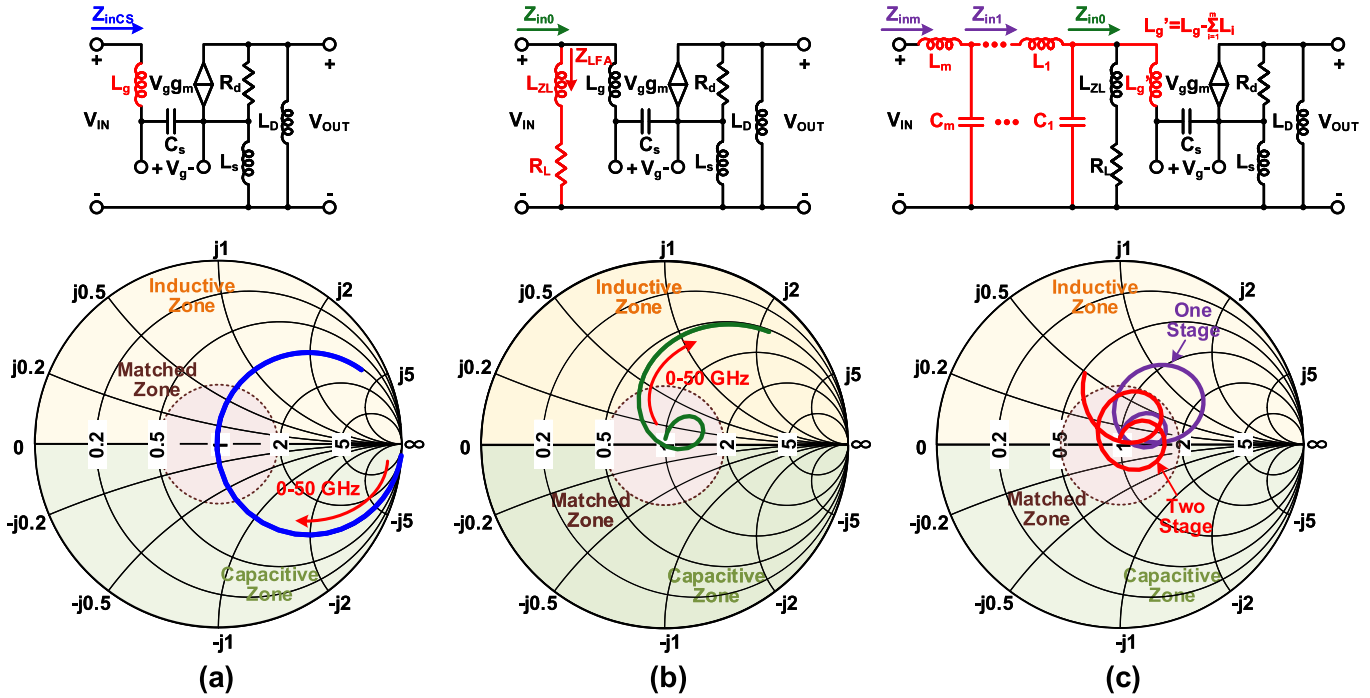

Fig. 4. Equivalent circuit and calculated input impedance of (a) conventional CS amplifier, (b) CS amplifier with low-frequency signal absorption network, and (c) reflectionless amplifier with one or two stages of distributed LC networks. $L_d = 800$ pH, $L_s = 150$ pH, $L_g = 600$ pH, $C_s = 100$ fF, $R_d = 180\ \Omega$, $g_m = 40$ ms, and $C_1 = C_2 = 60$ fF. $L_1 = L_g' = 300$ pH is used in the calculation of Z_{in1}, while in the calculation of Z_{in2}, $L_1 = L_2 = L_g' = 200$ pH is used as an example.

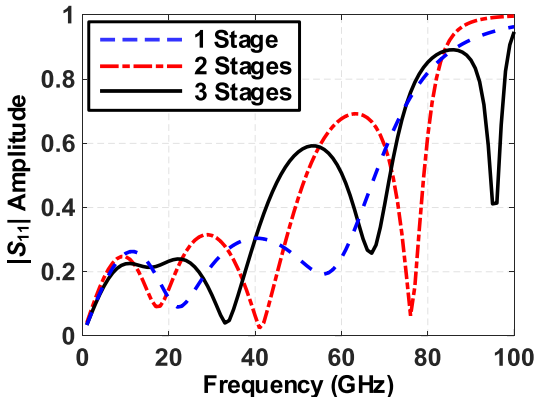

Fig. 5. Calculated S_{11} of reflectionless amplifier in a different number of distributed LC stages. The parameters used in the calculation are given in Fig. 4, and $L_1 = L_2 = L_3 = L_g' = 150$ pH are used in the calculation.

mixer and IF amplifier, a simple model of a nonlinear system is shown in Fig. 2. Such a nonlinear system consists of a nonlinear device connected to a linear network. Considering the nonlinear device with three harmonics, the nonlinear S-parameter (i.e., S_{A}) can be expressed as [25]

$$S_{\text{A}} = \begin{bmatrix} S'_{\text{A11}} & S'_{\text{A12}} \\ S'_{\text{A21}} & S'_{\text{A22}} \end{bmatrix} \tag{1}$$

where

$$S'_{\text{A}ij} = \begin{bmatrix} S_{\text{A}ij11} & S_{\text{A}ij12} & S_{\text{A}ij13} \\ S_{\text{A}ij21} & S_{\text{A}ij22} & S_{\text{A}ij23} \\ S_{\text{A}ij31} & S_{\text{A}ij32} & S_{\text{A}ij33} \end{bmatrix}. \tag{2}$$

For each parameter $S_{\text{A}ijkl}$, i and j refer to the output and input ports, respectively, while k and l are the harmonic indexes of output and input waves, respectively. As shown in Fig. 2, assuming that the nonlinear device is connected to a unidirectional linear network with ideal unity gain and an input reflection coefficient of Γ, then, the S-parameter of the linear network S_{B} and the transmission coefficient of the whole system (i.e., S_{T21}) [26] can be derived as follows:

$$S_{\text{B}} = \begin{bmatrix} S_{\text{B11}} & S_{\text{B12}} \\ S_{\text{B21}} & S_{\text{B22}} \end{bmatrix} = \begin{bmatrix} \Gamma & 0 \\ 1 & 0 \end{bmatrix} \tag{3}$$

$$S_{\text{T21}} = \begin{bmatrix} S_{\text{T2111}} & S_{\text{T2112}} & S_{\text{T2113}} \\ S_{\text{T2121}} & S_{\text{T2122}} & S_{\text{T2123}} \\ S_{\text{T2131}} & S_{\text{T2132}} & S_{\text{T2133}} \end{bmatrix} = S_{\text{B21}}\left(I - S'_{\text{A22}}S_{\text{B11}}\right)^{-1}S'_{\text{A21}}. \tag{4}$$

Here, the Γ matrix for linear network is expressed as

$$\Gamma = \begin{bmatrix} \Gamma_1 & 0 & 0 \\ 0 & \Gamma_2 & 0 \\ 0 & 0 & \Gamma_3 \end{bmatrix} \tag{5}$$

where Γ_n is the reflection coefficients of n-order harmonic. To simplify the analysis, assume that the nonlinear device with unity gain provides ideal isolation and input matching (i.e., $S'_{\text{A11}} = S'_{\text{A12}} = 0$). The nonlinear responses to the input signal

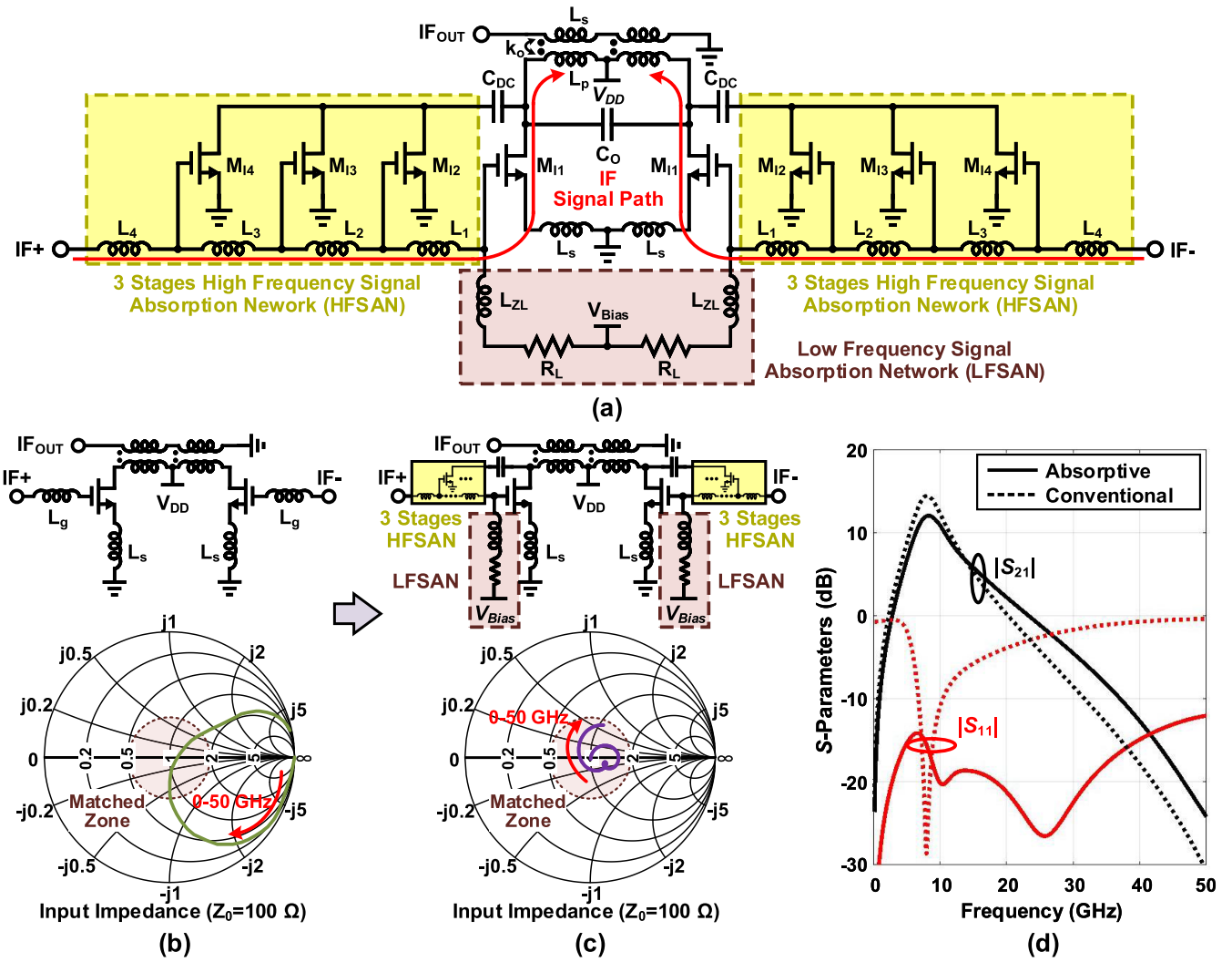

Fig. 6. (a) Schematic of the proposed absorptive IF amplifier. (b) Schematic and simulated input impedance of the conventional CS amplifier. (c) Schematic and simulated input impedance of the conventional CS amplifier with low- and high-frequency signal absorption networks. (d) Simulated S-parameter of the conventional amplifier and the proposed absorptive amplifier.

and reflected signal are expressed as

$$S'_{A21} = \begin{bmatrix} 1 & n_{t12} & n_{t13} \\ n_{t21} & 1 & n_{t23} \\ n_{t31} & n_{t32} & 1 \end{bmatrix} \tag{6}$$

$$S'_{A22} = \begin{bmatrix} 0 & n_{r12} & n_{r13} \\ n_{r21} & 0 & n_{r23} \\ n_{r31} & n_{r32} & 0 \end{bmatrix} \tag{7}$$

where n_t and n_r are the nonlinear coefficients of transmission and reflection signals, respectively. The output of a nonlinear system (i.e., b_k, where k is the harmonic index of output wave) can be calculated by the input wave (i.e., a_l, where l is the harmonic index of input wave) and the nonlinear S-parameter of the system, which is expressed as $b = S_T a$ [25]. Therefore, from a linear source with only fundamental signal output, i.e., $a = (1, 0, 0)^T$, the output wave of the nonlinear system can be derived as

$$\begin{bmatrix} b_1 \\ b_2 \\ b_3 \end{bmatrix} = S_{T21} \begin{bmatrix} 1 \\ 0 \\ 0 \end{bmatrix} = \begin{bmatrix} S_{T2111} \\ S_{T2121} \\ S_{T2131} \end{bmatrix}. \tag{8}$$

Here, b_1 is the fundamental signal output of the system, while the physical meanings of b_2 and b_3 are the second- and third-order harmonics generated from the fundamental input signal, respectively. Two reflective networks (i.e., Cases 1 and 2) and one reflectionless network of Case 3 are directly connected to the nonlinear device (i.e., S_A), as shown in Fig. 3(a). The calculated results show that the nonlinear responses b_2 and b_3 are varied with frequency in Cases 1 and 2, while Case 1 shows improved nonlinear response compared to other cases. However, the interconnection is required in the circuit implementation. Once the interconnection is taken into consideration, the nonlinear responses in Cases 1 and 2 are degraded rapidly in some frequencies, as shown in Fig. 3(b). Therefore, any reflection would cause unpredictable linearity degeneration in circuit implementation, while the reflectionless operation can eliminate such linearity degeneration in a nonlinear system.

B. Absorptive IF Amplifier

The absorptive IF amplifier with bandpass response can absorb the out-of-band signals without reflecting them back to

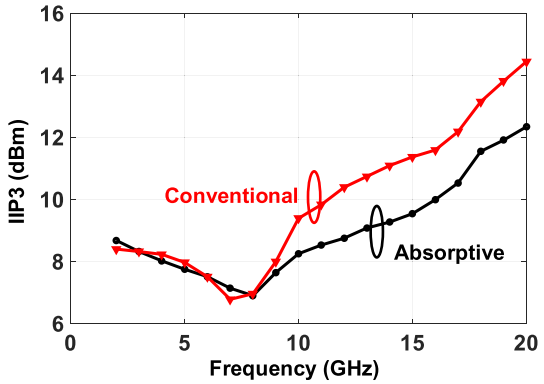

Fig. 7. Simulated IIP3 of the conventional IF amplifier and the proposed absorptive IF amplifier.

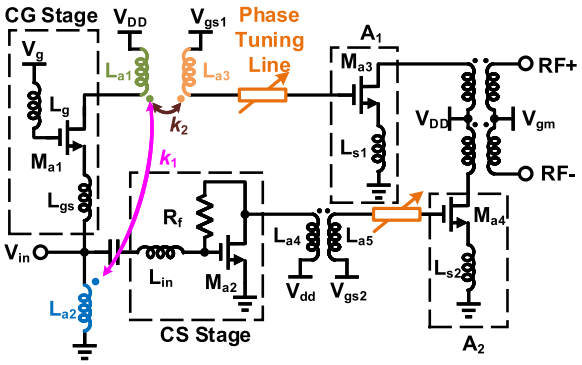

Fig. 8. Schematic of the proposed dual-path noise-canceling LNA. ($g_{ma1} = g_{ma2} = 40$ mS.)

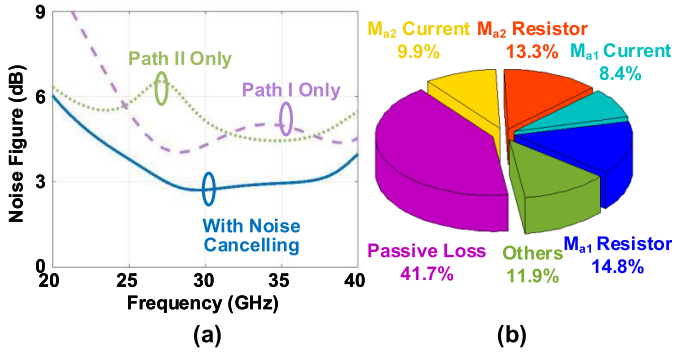

Fig. 9. (a) Simulated NF of the proposed LNA. (b) Simulated noise contribution of the proposed LNA at 30 GHz.

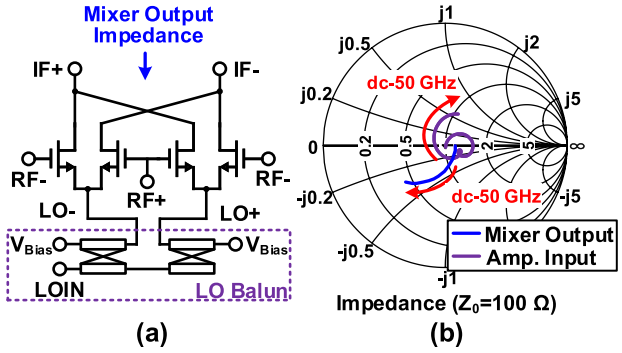

Fig. 10. (a) Schematic of the proposed mixer. (b) Simulated output impedance of the mixer and the input impedance of the proposed absorptive IF amplifier.

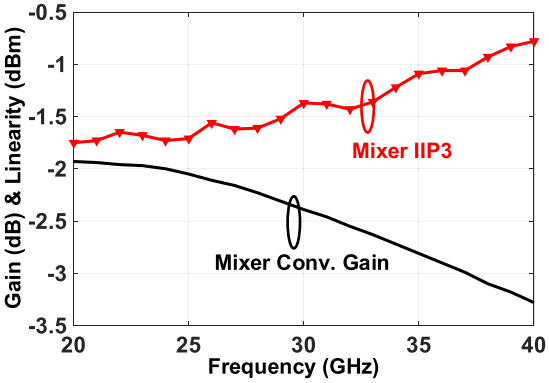

Fig. 11. Simulated gain and IIP3 of the proposed mixer ($P_{LO} = 3$ dBm).

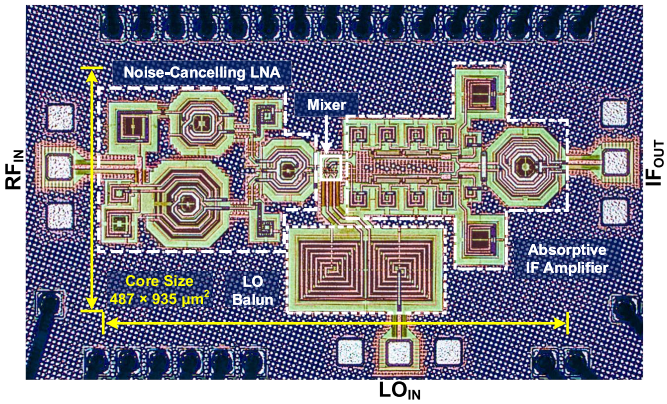

Fig. 12. Chip micrograph of the fabricated reflectionless RX.

the mixer. Thus, the linearity degeneration is mitigated based on the aforementioned analysis. In general, such reflectionless operation can be achieved once the mixer and absorptive amplifier are matched to 50 Ω simultaneously.

As shown in Fig. 4(a), the common-source (CS) topology is introduced in this design, while the inductor L_g is used to achieve impedance matching at passband frequency. Then, the Z-parameter can be expressed as (9), as shown at the bottom of the next page, where

$$A = R_d + s(L_d + L_s) \tag{10}$$

$$L_t = L_g + L_s \tag{11}$$

$$s = j\omega. \tag{12}$$

The input impedance (i.e., Z_{inCS}) can be calculated from the Z-parameters. The Smith chart of the calculated input impedance is shown in Fig. 4(a), which can be split into three zones.

1) The input impedance at lower frequency is located at the capacitance zone.
2) The input impedance at passband frequency is in the matched zone.
3) At higher frequency, the input impedance is in the inductance zone.

Two signal absorption networks are introduced to the proposed absorptive amplifier, which can not only absorb the out-of-band signal but also shift the input impedance from the

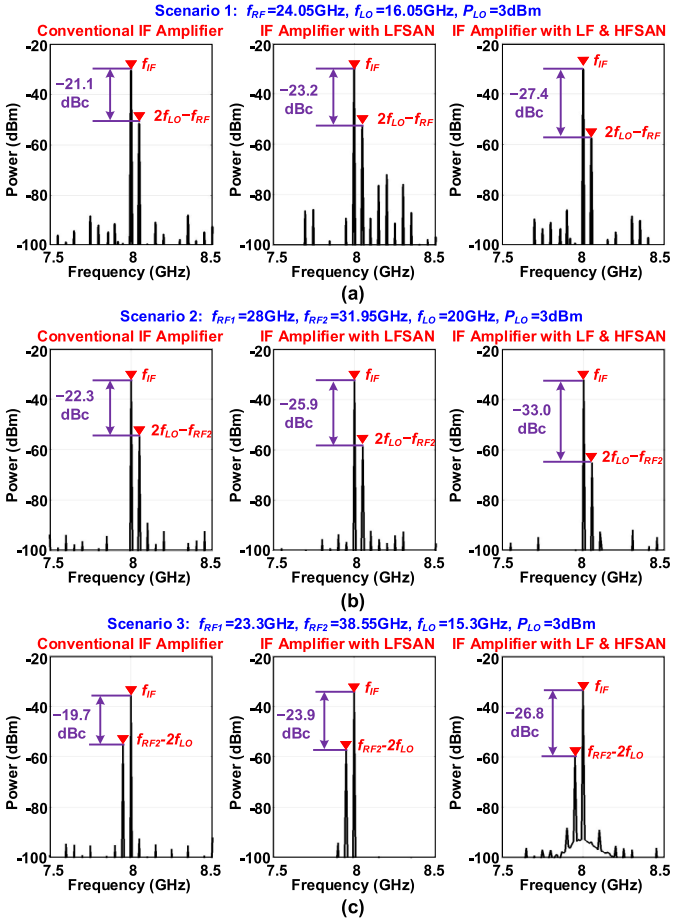

Fig. 13. Simulated output spectrum of the proposed RX with different IF amplifier configurations. (a) Single RF input with $f_{\mathrm{RF}} = 24.05$ GHz and $f_{\mathrm{LO}} = 16.05$ GHz. (b) Two RF inputs with $f_{\mathrm{RF1}} = 28$ GHz, $f_{\mathrm{RF2}} = 31.95$ GHz, and $f_{\mathrm{LO}} = 20$ GHz. (c) Two RF inputs with $f_{\mathrm{RF1}} = 23.3$ GHz, $f_{\mathrm{RF2}} = 38.55$ GHz, and $f_{\mathrm{LO}} = 15.3$ GHz.

capacitance zone and inductance zone to the matched zone at lower and higher frequencies, respectively. Here, an inductor L_{ZL} in series connected with a loaded resistor R_L is introduced as a low-frequency signal absorption network in the input port of the CS amplifier, as shown in Fig. 4(b). The low-frequency signal is transmitted and consumed in the loaded resistor. Then, the input impedance of the CS amplifier with a low-frequency signal absorption network can be expressed as

$$Z_{\mathrm{in0}} = \frac{Z_{\mathrm{inCS}} Z_{\mathrm{LFA}}}{Z_{\mathrm{inCS}} + Z_{\mathrm{LFA}}} \tag{13}$$

where the input impedance of low-frequency absorption network Z_{LFA} is

$$Z_{\mathrm{LFA}} = sL_{\mathrm{ZL}} + R. \tag{14}$$

The calculated result in Fig. 4(b) shows that the input impedance at lower frequency is shifted to the matched zone.

TABLE I

COMPONENT VALUES OF THE ABSORPTIVE AMPLIFIER AT 8 GHz

Device	M_{I1}	M_{I2}	M_{I3}	M_{I4}	$L_{1,2,3}$	L_4	L_s
Value	115 μm/ 30 nm	11 μm/ 30 nm	24 μm/ 30 nm	42 μm/ 30 nm	95 pH	110 pH	30 pH
Device	L_{ZL}	R_L	C_O	C_{DC}	L_p	L_s	k_o
Value	550 pH	50 Ω	250 fF	120 fF	480 pH	370 pH	0.65

TABLE II

BIAS CURRENT AND VOLTAGES OF THE ACTIVE DEVICES

Device	M_{a1}	M_{a2}	M_{a3}	M_{a4}	M_{I1}	
Current (mA)	5.3	5.1	6.0	4.0	7.8	
Voltage	V_{DD}	V_g	V_{gs1}	V_{gs2}	V_{gm}	V_{Bias}
Value (mV)	900	520	490	500	840	440

To further achieve a wideband reflectionless operation, the input inductor L_g can be replaced by a distributed LC network, which can shift the inductive impedance to the matched zone at a higher frequency, as shown in Fig. 4(c). The input impedance of the absorptive amplifier with m-stages distributed LC network can be expressed as

$$Z_{\mathrm{in}m} = sL_m + \frac{Z_{\mathrm{in}(m-1)}}{sC_m Z_{\mathrm{in}(m-1)} + 1} \quad (m = 1, 2, 3\ldots). \tag{15}$$

As shown in Fig. 5, each stage of distributed LC network can introduce a transmission pole to the matching network of absorptive amplifier. Therefore, the reflectionless range can be extended by increasing the number of distributed LC stages. Meanwhile, Fig. 4(c) shows that the impedance matching at higher frequency can be improved by increasing the number of LC stages. Therefore, based on the aforementioned mechanisms, the design procedures of the proposed absorptive IF amplifier can be summarized as follows.

1) A CS amplifier operated at the IF frequency is designed.
2) The low-frequency signal absorption network is taped to the input matching network of the IF amplifier, where the resistance of R_L is equal to the terminal impedance and the inductance of L_{ZL} is chosen to allocate the input impedance to the matching zone in the lower side of IF frequency.
3) The distributed LC network is used to replace the input matching inductor, which forms the high-frequency signal absorption network.

The bandwidth with good impedance matching in the higher frequency is determined by the number of distributed LC stages, while the capacitance and inductance of each stage are optimized to achieve improved reflectionless operation based on (15).

$$[Z] = \begin{bmatrix} \dfrac{A + sL_s R_d{}^2 g_m + s^2 C_s L_t R_d + s^3 C_g \left(L_g L_s + L_d L_t\right)}{sAC_g} & \dfrac{s^2 L_d L_s}{A} \\ \dfrac{L_d\left(-g_m R_d + s^2 L_s C_g\right)}{ac_g} & \dfrac{sL_d(R_d + sL_s)}{A} \end{bmatrix} \tag{9}$$

III. Implementation

A. Absorptive IF Amplifier

Based on the principle analyzed in Section II, an absorptive differential amplifier operated at 8 GHz is designed and implemented, as shown in Fig. 6(a). The absorptive IF amplifier consists of three parts.

1) Part I is a conventional CS amplifier with output matching network (i.e., output transformer and a capacitor C_O) as the IF signal path.
2) Part II is an inductor L_{ZL} loaded with a resistor R_L as a low-frequency signal absorption network. Here, the bias voltage of the CS amplifier stages (i.e., V_{bias}) is fed by the R_L.
3) Part III is a distributed FET array connected with four inductors as the high-frequency signal absorption network.

To verify the aforementioned structures, a 28-nm CMOS technology is used. Fig. 6(b) shows the schematic of the conventional CS amplifier. The input impedance is matched to 100 Ω by an inductor $L_g = 600$ pH, while a source degeneration inductor $L_s = 80$ pH is utilized to improve the stability of the CS amplifier. The simulated input impedance in Fig. 6(b) shows that the impedance matching is achieved at passband frequency. Then, the inductor $L_{ZL} = 550$ pH loaded with a resistor $R_L = 50$ Ω is utilized as a low-frequency signal absorption network in the proposed absorptive amplifier. Meanwhile, a high-frequency signal absorption network with three-stage distributed LC networks is designed. Here, the capacitors in the LC network are implemented using the low-Q junction capacitor of transistor. Such a low-Q capacitor can improve the signal absorption capability at a higher frequency without significantly degenerating the IF passband. Thus, as shown in Fig. 6(c), good impedance matching is achieved from dc to 50 GHz.

Table I shows the optimized component values of the proposed absorptive amplifier. The simulated S-parameters in Fig. 6(d) reveals that compared to the conventional amplifier, the out-of-band S_{11} is much lower, while minor variations on the S_{21} are exhibited in the proposed amplifier. Meanwhile, Fig. 7 reveals that the linearity of the proposed absorptive IF amplifier shows little degeneration compared to the conventional IF amplifier.

B. Dual-Path Noise-Canceling LNA

Fig. 8 shows the schematic of the proposed dual-path noise-canceling LNA [27]. The wideband input matching is mainly achieved by the common-gate (CG) stage with inductor L_{gs}, while a dc-block capacitor is used in the input of CS stage. Meanwhile, the phase-tuning lines [28] are introduced in the proposed LNA to calibrate the phase variation caused by process, voltage, and temperature (PVT) issues, which improves the noise-canceling performance. The output of both paths is connected to an optimized output transformer with high common-mode rejection ratio, and such a transformer can not only reduce the common-mode noise but also provide the wideband impedance matching between the LNA and the mixer.

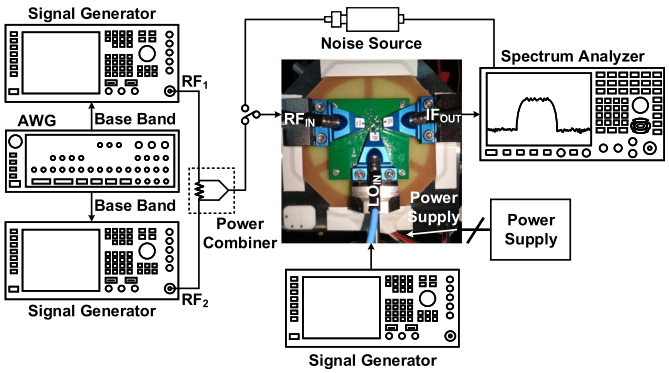

Fig. 14. Test setup.

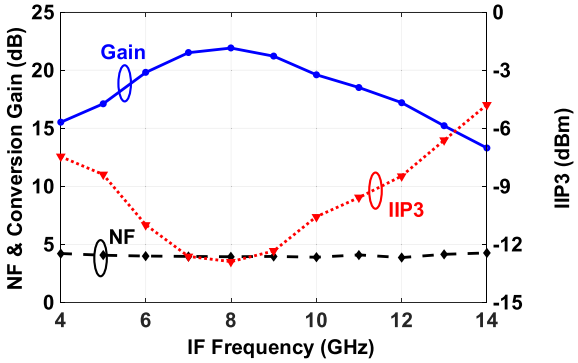

Fig. 15. Measured conversion gain, NF, and IIP3 versus IF frequency ($f_{RF} = 28$ GHz and f_{LO} is varied from 14 to 24 GHz for IF frequency from 14 to 4 GHz).

Fig. 9(a) shows that the noise of paths I and II can be reduced simultaneously in the proposed noise-canceling LNA. Note that the fully noise-canceling condition could not be satisfied within a wide frequency range in the proposed dual-path noise-canceling LNA since the noise-canceling ratio is varied with the frequency-dependent inductance and capacitance. Therefore, the component values in the proposed LNA are optimized to achieve improved NF, which results in a partial noise-canceling operation in both CG and CS paths [27]. The noise contribution in Fig. 9(b) reveals that the noise introduced by the current of M_{a1} and M_{a2} is only about 8.4% and 9.9%, respectively, while the noise is mostly contributed by the passive loss and parasitic resistor of M_{a1} and M_{a2} (i.e., gate bias-independent resistance r_{gbi}, source parasitic resistance r_s, and drain parasitic resistance r_d).

C. Mixer

Based on the analysis in Section II, the mixer is matched to the absorptive IF amplifier in a wide frequency range, which achieves the reflectionless operation between the mixer and the IF amplifier. Therefore, the double-balance passive mixer is designed, as shown in Fig. 10(a). Such mixer can reduce the LO and RF signal leakage, while the mixer is configured in source-pumped mode due to the lower conversion loss [29]. Meanwhile, an additional on-chip LO balun [30] is implemented for differential LO generation. The simulated result in Fig. 10(b) is obtained from the post-layout simulation with LO balun connected to the mixer, which shows that the output impedance of the mixer is well matched with the input

TABLE III
PERFORMANCE SUMMARY AND COMPARISON WITH STATE-OF-THE-ART RXS

Ref.	**This Work**	ISSCC 2018 [31]	ISSCC 2019 [14]	JSSC 2019 [6]	ISSCC 2020 [15]	TMTT 2020 [32]
Architecture	**Reflectionless Heterodyne**	Heterodyne	ASF^{+} Based Blocker Rejection	Cartesian-Combined Image Rejection	Harmonic-Mixing Based Beam-Space	Heterodyne
Technology	**28-nm CMOS**	28-nm CMOS	45-nm CMOS SOI	65-nm CMOS	65-nm CMOS	65-nm CMOS
Frequency (GHz)	**22.6–39.2**	26.5–29.5	27–41	27–30 / 35–39	28	26.5–32.5
Conv. Gain (dB)	**19.5–22.5**	32–34$^{\diamond}$	36	33 / 26.5	>16	26.5–29.5
Noise Figure (dB)	**3.6–5**	4.4–4.7	4.3–6.3	5.7 / 8.5	6–7.8	5.3–6.3
IP_{1dB} (dBm)	**>−23**	N/A	−34	−30 / −23	−36.9	−28
IIP3 (dBm)	**>−14.2**	N/A	−25	N/A	N/A	N/A
Modulation Data-Rate, EVM	**256-QAM 3.6 Gb/s, 1.58% 1024-QAM 1.5 Gb/s, 1.4%**	64-QAM 2.4 Gb/s, <5.6%	N/A	N/A	64-QAM 0.9 Gb/s, 6.2%	N/A
Modulation Data-Rate, EVM After Blocker/Interference Rejection	**256-QAM 0.8 Gb/s, <3.43% 50MHz Overlap**	N/A	64-QAM 3.0 Gb/s, 3.7% 256-QAM 0.8 Gb/s, 2.3%	N/A	16-QAM 0.4 Gb/s, 9.7%	N/A
DC Power (mW)	**33**	42	<85	52.5	112.5$^{\diamond\diamond}$	33
Core area (mm^2)	**0.46**	1.16$^{\#}$	1.85*	0.32	0.66	0.48

$^{\diamond}$ 4 channels combined. $^{\#}$ Single channel transceiver. $^{+}$ Autonomous spatial filter. * Estimated single channel. $^{\diamond\diamond}$ Single element with four output steams.

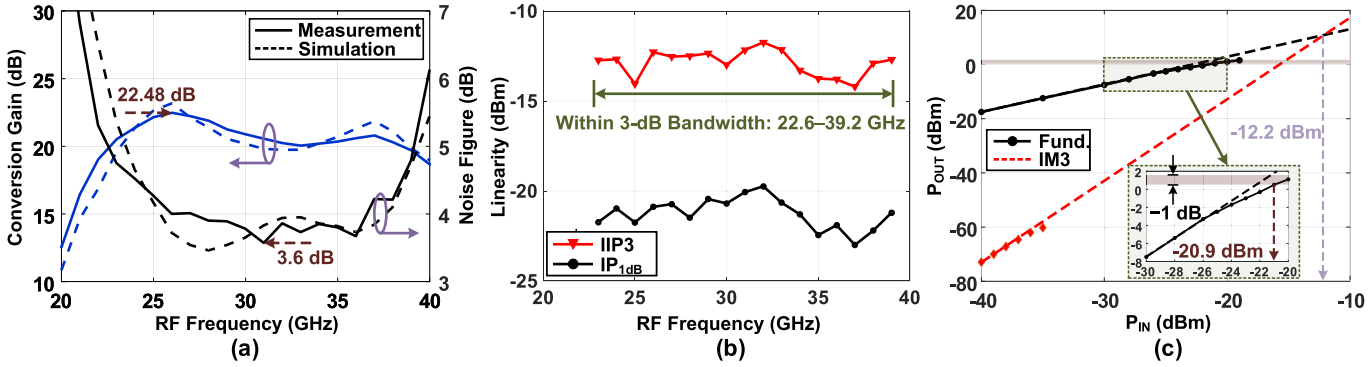

Fig. 16. (a) Simulated and measured gain and NF of the proposed reflectionless RX. (b) Measured linearity of the proposed reflectionless RX. (c) Measured linearity of the proposed reflectionless RX at 26 GHz.

impedance of absorptive IF amplifier. Therefore, the output-of-band signal reflection can be reduced between the mixer and absorptive IF amplifier. Meanwhile, Fig. 11 shows that the conversion gain and input third-order intercept point (IIP3) of the proposed mixer are relatively low, which limits the linearity of the proposed RX.

D. Reflectionless RX

Based on the mechanisms and circuits mentioned above, a reflectionless RX is implemented and fabricated using a conventional 28-nm CMOS technology. Fig. 12 shows the micrograph of the fabricated reflectionless RX, where the chip occupies a core area of 487 × 935 μm^2. Table II specifies the bias currents and voltages of the active devices. The proposed RX consumes 33 mW from a 0.9-V voltage supply (i.e., 19 mW in LNA and 14 mW in IF amplifier).

To investigate the influence of signal absorption networks on the in-band high-order mixing products, Fig. 13 shows the simulated output spectrum of the proposed RX with or without the absorptive networks at following three scenarios:

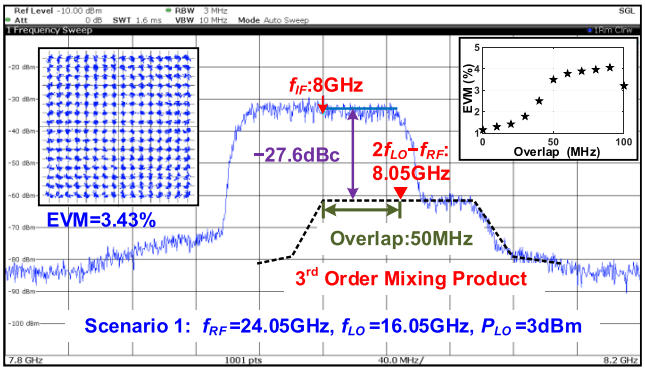

(a)

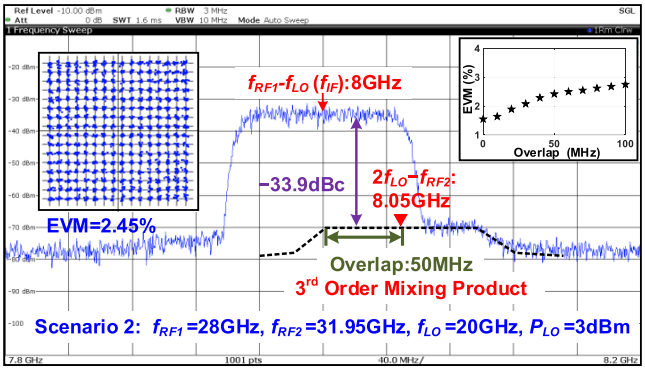

(b)

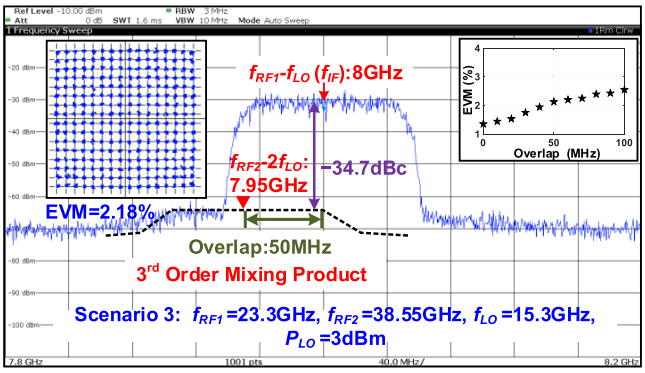

(c)

Fig. 17. Measured results of the proposed RX under the case of 100-MHz channel bandwidth, 256-QAM modulation, once the third-order mixing product of RF signal is 50-MHz overlap with the IF signal. (a) Single RF input with f_{RF} = 24.05 GHz and f_{LO} = 16.05 GHz. (b) Two RF inputs with f_{RF1} = 28 GHz, f_{RF2} = 31.95 GHz, and f_{LO} = 20 GHz. (c) Two RF inputs with f_{RF1} = 23.3 GHz, f_{RF2} = 38.55 GHz, and f_{LO} = 15.3 GHz. (P_{RF} and P_{LO} are identical for each setup.)

1) single RF input with f_{RF} = 24.05 GHz and f_{LO} = 16.05 GHz;
2) two RF inputs with f_{RF1} = 28 GHz, f_{RF2} = 31.95 GHz, and f_{LO} = 20 GHz;
3) two RF inputs with f_{RF1} = 23.3 GHz, f_{RF2} = 38.55 GHz, and f_{LO} = 15.3 GHz.

The simulated results reveal that both low- and high-frequency signal absorption networks can reduce the in-band third-order mixing products. Meanwhile, by using the proposed signal absorption networks, the 6.3-, 10.7-, and 7.1-dB improvements on the suppression of in-band third-order mixing products are achieved in scenarios 1–3, respectively.

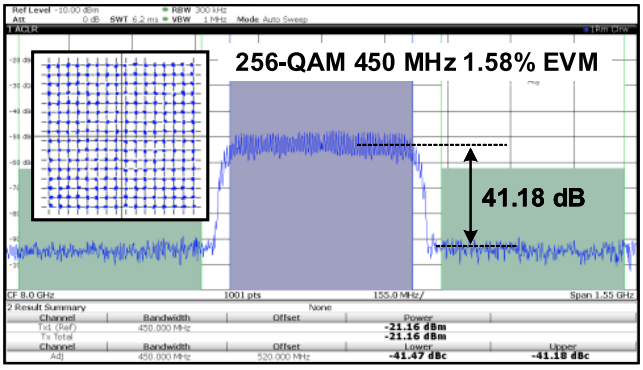

(a)

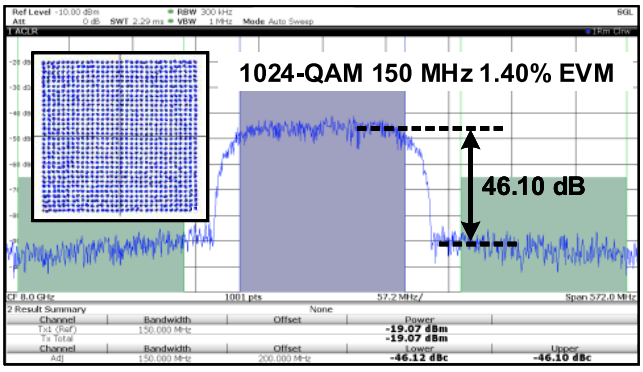

(b)

Fig. 18. Measured output spectrum and constellation diagram of the proposed RX at f_{RF} = 28 GHz. (a) 256-QAM, 450 MHz. (b) 1024-QAM, 150 MHz.

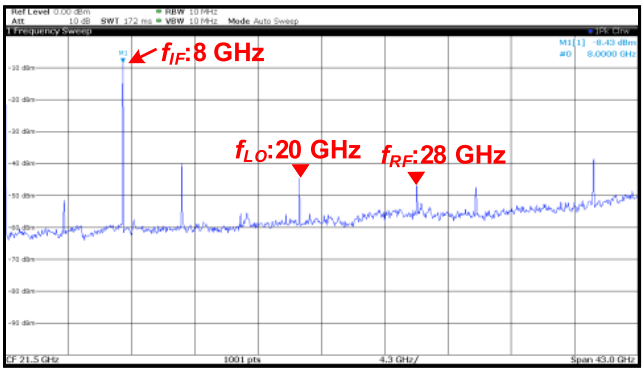

Fig. 19. Measured output spectrum of the proposed RX at f_{RF} = 28 GHz.

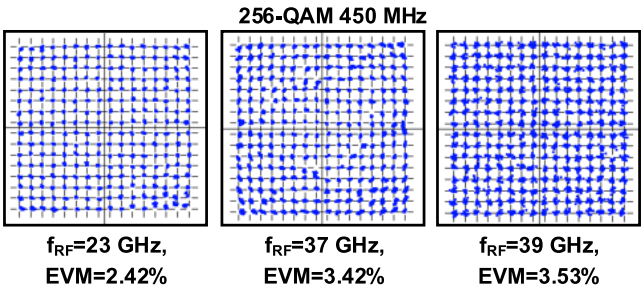

Fig. 20. Measured constellation diagram of the proposed RX at f_{RF} = 23, 37, and 39 GHz.

IV. Measured Results

To verify the aforementioned structures, the fabricated chip is measured using the test setup shown in Fig. 14. Two signal sources and spectrum analyzer are used in the measurement of the RX gain and linearity performance. The signal source can

generate the modulation signal using the external baseband signal, while the required baseband signal is provided by an AWG. To measure the NF of the proposed LNA, the spectrum analyzer with noise analyzer function and a noise source are used. During the measurement, the LO power is 3 dBm. Fig. 15 shows that the measured 1-dB IF bandwidth is about 7–9 GHz, while the NF shows little variation versus IF frequency. Therefore, $f_{\mathrm{IF}} = 8$ GHz is assigned to achieve the improved performance. Fig. 16(a) shows that the peak conversion gain is 22.48 dB at 26 GHz with the 3-dB bandwidth of 22.6–39.2 GHz. Meanwhile, the measured minimum NF is 3.6 dB at 31 GHz and the NF is lower than 5 dB in 22.5–39.4 GHz, as shown in Fig. 16(a). Besides, Fig. 16(b) reveals that the input 1-dB compression point ($\mathrm{IP}_{1\,\mathrm{dB}}$) is from -23 to -19.7 dBm, while the IIP3 is from -14.2 to -11.7 dBm over the 3-dB operation bandwidth of 22.6–39.2 GHz. Here, $\mathrm{IP}_{1\,\mathrm{dB}}$ of -20.9 dBm and IIP3 of -12.2 dBm are measured at the maximum gain frequency of 26 GHz, as shown in Fig. 16(c).

To verify the advantage of the proposed reflectionless RX, the modulation signal measurement is performed at three scenarios shown in Fig. 13. Fig. 17(a) shows that the -27.6-, -33.9-, and -34.7-dBc third-order mixing products are measured in the aforementioned scenarios. Once the third-order mixing product is 50-MHz overlap with the IF signal, the proposed RX can still support 100-MHz, 256-quadratic amplitude modulation (QAM) modulation signal, while Fig. 17 shows that the measured error vector magnitudes (EVMs) are 3.43%, 2.75%, and 2.18% in three scenarios. Here, the overlap bandwidth is varied with the frequency of f_{LO} and f_{RF}, while the measured EVM is degraded from 1.16% (0-MHz overlap) to 4.06% (90-MHz overlap) in scenario 1, as shown in Fig. 17(a). The EVM at 100-MHz overlap is improved in scenario 1 since the third-order mixing products and IF signal carry the same baseband signal. Meanwhile, as shown in Fig. 17(b) and (c), the EVM is decreased from 1.55% (0 MHz overlap) to 2.78% (100 MHz overlap) and from 1.35% (0 MHz overlap) to 2.54% (100 MHz overlap) in scenarios 2 and 3, respectively. Therefore, the measurement proves that the proposed reflectionless RX can support high-speed communication in a complex EM environment.

Under the case of $f_{\mathrm{RF}} = 28$ GHz and $f_{\mathrm{LO}} = 20$ GHz, the RX does not suffer from the interference caused by the high-order mixing products. The measured output spectrum and the constellation diagram of the proposed reflectionless RX are shown in Fig. 18. The RX can support 3.6-Gb/s 256-QAM and 1.5-Gb/s 1024-QAM modulation signals with the SNRs of 41.18 and 46.10 dB, respectively.

Fig. 19 shows that the output spectrum of the proposed reflectionless RX is clean, while most of the intermodulation or high-order mixing products are suppressed. Meanwhile, Fig. 20 reveals that the proposed reflectionless RX can support high data rate within the operating frequency range.

The performance summary and comparison with the state of the arts are shown in Table III. To the authors' best knowledge, this article presents the first RX using the reflectionless mechanism to reduce the in-band interference caused by the high-order mixing products. Compared to previous mm-wave RXs, the proposed RX shows the state-of-the-art performances on the NF, linearity, power consumption, and supporting 1024-QAM modulation in a compact size.

V. Conclusion

In this article, a 22.6–39.2-GHz reflectionless RX is presented. Such RX can not only suppress the in-band interference using the reflectionless operation between the mixer and absorptive IF amplifier but also reduce the NF by the dual-path noise-canceling LNA. Then, the proposed reflectionless RX is fabricated in a conventional 28-nm CMOS technology and measured for verification. The proposed RX can improve the in-band high-order mixing products suppression, hence supporting high-speed communication in a complex EM environment. Meanwhile, the measurement shows that the peak gain is 22.5 dB, while the minimum NF is 3.6 dB. Besides, the proposed RX can support multi-Gb/s, 256-/1024-QAM modulations. Therefore, the proposed reflectionless RX is attractive for wideband mm-wave wireless applications (e.g., 5G).

References

[1] C.-N. Chen, Y. Chen, Y. Wang, T.-Y. Kuo, and H. Wang, "38-GHz CMOS linearized receiver with IM3 suppression, $P_{1\ dB}$/IP3/RR3 enhancements, and mitigation of QAM constellation diagram distortion in 5G MMW systems," *IEEE Trans. Microw. Theory Techn.*, vol. 68, no. 7, pp. 2779–2795, Jul. 2020.

[2] Y. Yoon *et al.*, "A highly linear 28 GHz 16-element phased-array receiver with wide gain control for 5G NR application," in *Proc. IEEE Radio Freq. Integr. Circuits Symp. (RFIC)*, Jun. 2019, pp. 287–290.

[3] F. Bruccoleri, E. A. M. Klumperink, and B. Nauta, "Wide-band CMOS low-noise amplifier exploiting thermal noise canceling," *IEEE J. Solid-State Circuits*, vol. 39, no. 2, pp. 275–282, Feb. 2004.

[4] H. Yu, Y. Chen, C. C. Boon, P.-I. Mak, and R. P. Martins, "A 0.096-mm^2 1–20-GHz triple-path noise- canceling common-gate common-source LNA with dual complementary pMOS–nMOS configuration," *IEEE Trans. Microw. Theory Techn.*, vol. 68, no. 1, pp. 144–159, Jan. 2020.

[5] L. Gao, Q. Ma, and G. M. Rebeiz, "A 20–44-GHz image-rejection receiver with >75-dB image-rejection ratio in 22-nm CMOS FD-SOI for 5G applications," *IEEE Trans. Microw. Theory Techn.*, vol. 68, no. 7, pp. 2823–2832, Jul. 2020.

[6] S. Mondal and J. Paramesh, "A reconfigurable 28-/37-GHz MMSE-adaptive hybrid-beamforming receiver for carrier aggregation and multi-standard MIMO communication," *IEEE J. Solid-State Circuits*, vol. 54, no. 5, pp. 1391–1406, May 2019.

[7] M.-Y. Huang, T. Chi, F. Wang, S. Li, T.-Y. Huang, and H. Wang, "A 24.5–43.5 GHz compact RX with calibration-free 32–56 dB full-frequency instantaneously wideband image rejection supporting multi-Gb/s 64-QAM/256-QAM for multi-band 5G massive MIMO," in *Proc. IEEE Radio Freq. Integr. Circuits Symp. (RFIC)*, Jun. 2019, pp. 275–278.

[8] N. Ebrahimi and J. F. Buckwalter, "A high-fractional-bandwidth, millimeter-wave bidirectional image-selection architecture with narrow-band LO tuning requirements," *IEEE J. Solid-State Circuits*, vol. 53, no. 8, pp. 2164–2176, Aug. 2018.

[9] T. H. Jang *et al.*, "120-GHz wideband I/Q receiver based on baseband equalizing technique," *IEEE J. Solid-State Circuits*, vol. 56, no. 6, pp. 1697–1710, Jun. 2021.

[10] A. Ahmed, M.-Y. Huang, D. Munzer, and H. Wang, "A 43–97-GHz mixer-first front-end with quadrature input matching and on-chip image rejection," *IEEE J. Solid-State Circuits*, vol. 56, no. 3, pp. 705–714, Mar. 2021.

[11] M.-Y. Huang, T. Chi, S. Li, T.-Y. Huang, and H. Wang, "A 24.5–43.5-GHz ultra-compact CMOS receiver front end with calibration-free instantaneous full-band image rejection for multiband 5G massive MIMO," *IEEE J. Solid-State Circuits*, vol. 55, no. 5, pp. 1177–1186, May 2020.

[12] S. Jain, Y. Wang, and A. Natarajan, "A 10 GHz CMOS RX frontend with spatial cancellation of co-channel interferers for MIMO/digital beamforming arrays," in *Proc. IEEE Radio Freq. Integr. Circuits Symp. (RFIC)*, May 2016, pp. 99–102.
[13] L. Zhang and H. Krishnaswamy, "Arbitrary analog/RF spatial filtering for digital MIMO receiver arrays," *IEEE J. Solid-State Circuits*, vol. 52, no. 12, pp. 3392–3404, Dec. 2017.
[14] M.-Y. Huang and H. Wang, "21.2 A 27-to-41GHz MIMO receiver with N-input-N-output using scalable cascadable autonomous array-based high-order spatial filters for instinctual full-FoV multi-blocker/signal management," in *IEEE ISSCC Dig. Tech. Papers*, Feb. 2019, pp. 346–347.
[15] R. Garg *et al.*, "A 28 GHz 4-element MIMO beam-space array in 65 nm CMOS with simultaneous spatial filtering and single-wire frequency-domain multiplexing," in *IEEE ISSCC Dig. Tech. Papers*, Feb 2020, pp. 80–81.
[16] E. Ghaderi, A. S. Ramani, A. A. Rahimi, D. Heo, S. Shekhar, and S. Gupta, "Four-element wide modulated bandwidth MIMO receiver with >35-dB interference cancellation," *IEEE Trans. Microw. Theory Techn.*, vol. 68, no. 9, pp. 3930–3941, Sep. 2020.
[17] M.-Y. Huang, T. Chi, F. Wang, T.-W. Li, and H. Wang, "A 23-to-30 GHz hybrid beamforming MIMO receiver array with closed-loop multistage front-end beamformers for full-FoV dynamic and autonomous unknown signal tracking and blocker rejection," in *IEEE ISSCC Dig. Tech. Papers*, Feb. 2018, pp. 68–69.
[18] M. A. Morgan, *Reflectionless Filters*. Norwood, MA, USA: Artech House, 2017.
[19] B. Mini-Circuits, "Reflectionless filters improve linearity and dynamic range," *Microw. J.*, vol. 58, no. 8, pp. 42–50, Aug. 2015.
[20] M. A. Morgan and T. A. Boyd, "Theoretical and experimental study of a new class of reflectionless filter," *IEEE Trans. Microw. Theory Techn.*, vol. 59, no. 5, pp. 1214–1221, May 2011.
[21] C. Liu, Z. Deng, X. Liu, and X. Luo, "A wideband bandpass filter with broad stopband and ultra-wide reflectionless range for 5G applications," in *IEEE MTT-S Int. Microw. Symp. Dig.*, Jun. 2019, pp. 834–837.
[22] Z. Deng, H. J. Qian, and X. Luo, "A 3.6 dB NF, 23–39GHz reflectionless RX with absorptive amplifier and dual-path noise cancelling LNA supporting 64-QAM/256-QAM/1024-QAM for 5G NR," in *Proc. IEEE Custom Integr. Circuits Conf. (CICC)*, Apr. 2021, pp. 1–2.
[23] V. Bhagavatula, T. Zhang, A. R. Suvarna, and J. C. Rudell, "Ultra-wideband IF millimeter-wave receiver with a 20 GHz channel bandwidth using gain-equalized transformers," *IEEE J. Solid-State Circuits*, vol. 51, no. 2, pp. 323–331, Feb. 2016.
[24] Y.-C. Wu, Y.-J. Hwang, C.-C. Chiong, B.-Z. Lu, and H. Wang, "An innovative joint-injection mixer with broadband if and RF for advanced heterodyne receivers of millimeter-wave astronomy," *IEEE Trans. Microw. Theory Techn.*, vol. 68, no. 12, pp. 5408–5422, Dec. 2020.
[25] J. A. Jargon, K. C. Gupta, and D. C. DeGroot, "Nonlinear large-signal scattering parameters: Theory and applications," in *Proc. IEEE ARFTG 63rd Conf.*, Apr. 2004, pp. 157–174.
[26] C. Bachiller, H. E. Gonzalez, V. E. B. Esbert, A. B. Martinez, and J. V. Morro, "Efficient technique for the cascade connection of multiple two-port scattering matrices," *IEEE Trans. Microw. Theory Techn.*, vol. 55, no. 9, pp. 1880–1886, Sep. 2007.
[27] Z. Deng, J. Zhou, H. J. Qian, and X. Luo, "A 22.9–38.2-GHz dual-path noise-canceling LNA with 2.65–4.62-dB NF in 28-nm CMOS," *IEEE J. Solid-State Circuits*, vol. 56, no. 11, pp. 3348–3359, Nov. 2021.
[28] Z. Deng, J. Zhou, H. J. Qian, and X. Luo, "High resolution reconfigurable phase-tuning line using self-shielded 3-D interdigital capacitor," *IEEE Microw. Wireless Compon. Lett.*, vol. 30, no. 6, pp. 605–608, Jun. 2020.
[29] M. Bao, H. Jacobsson, L. Aspemyr, G. Carchon, and X. Sun, "A 9–31-GHz subharmonic passive mixer in 90-nm CMOS technology," *IEEE J. Solid-State Circuits*, vol. 41, no. 10, pp. 2257–2264, Oct. 2006.
[30] H. J. Qian and X. Luo, "Compact 6.5–28.5 GHz on-chip balun with enhanced inband balance responses," *IEEE Microw. Wireless Compon. Lett.*, vol. 26, no. 12, pp. 993–995, Dec. 2016.
[31] J. D. Dunworth *et al.*, "A 28 GHz bulk-CMOS dual-polarization phased-array transceiver with 24 channels for 5G user and basestation equipment," in *IEEE ISSCC Dig. Tech. Papers*, Feb. 2018, pp. 70–71.
[32] R. Singh, S. Mondal, and J. Paramesh, "A millimeter-wave receiver using a wideband low-noise amplifier with one-port coupled resonator loads," *IEEE Trans. Microw. Theory Techn.*, vol. 68, no. 9, pp. 3794–3803, Sep. 2020.

Zhixian Deng (Graduate Student Member, IEEE) received the B.E. degree in microelectronics science and engineering from the University of Electronic Science and Technology of China, Chengdu, China, in 2019, where he is currently pursuing the Ph.D. degree in electronic science and technology.

His research interests include the reconfigurable microwave/millimeter-wave transceiver and passive components, especially integrated circuits.

Mr. Deng was a recipient of the IEEE International Microwave Symposium (IMS) Student Design Competition Award from 2017 to 2019 and the 2022 IEEE Microwave Theory and Techniques (MTT)-Society Graduate Fellowship Award.

Huizhen Jenny Qian (Member, IEEE) received the B.E., master's, and Ph.D. degrees in electronic engineering from the University of Electronic Science and Technology of China (UESTC), Chengdu, China, in 2008, 2011, and 2018, respectively.

Since 2019, she has been a Faculty Member with the Center for Integrated Circuits, UESTC, where she is currently an Associate Professor. Her research interests include wideband microwave/millimeter-wave transceivers, reconfigurable passive circuits, and on-chip array systems.

Dr. Qian was a recipient/co-recipient of the IEEE International Symposium on Radio frequency Integration Technology (RFIT) Best Student Paper Award in 2016 and 2019, the IEEE International Wireless Symposium (IWS) Best Student Paper Award in 2015 and 2018, the IEEE IMS Student Design Competition Award in 2017 and 2018, and the 2018 IEEE MTT-Society Graduate Fellowship Award.

Xun Luo (Senior Member, IEEE) received the B.E. and Ph.D. degrees in electronic engineering from the University of Electronic Science and Technology of China (UESTC), Chengdu, China, in 2005 and 2011, respectively.

From 2010 to 2013, he was with Huawei Technologies Company Ltd., Shenzhen, China, as the Project Manager to guide research and development projects of multi-band microwave/millimeter-wave (mm-wave) integrated systems for backhaul and wireless communication. Before joining UESTC, he was an Assistant Professor with the Department of Microelectronics, Delft University of Technology, Delft, The Netherlands. Since 2015, he has been with UESTC as a Full Professor, where he has been appointed as the Executive Director of the Center for Integrated Circuits. Since 2020, he has been the Head of the Center for Advanced Semiconductor and Integrated Micro-System (ASIS), UESTC. He has authored or coauthored more than 100 journal articles and conference papers. He holds 44 patents. His research interests include RF/microwave/mm-wave integrated circuits, multiple-resonance terahertz (THz) modules, multi-bands backhaul/wireless systems, reconfigurable passive circuits, smart antenna, and system in package.

Dr. Luo is a Technical Program Committee Member of multiple IEEE conferences, including the IEEE Radio Frequency Integrated Circuits (RFIC) Symposium, and the IEEE MTT-Society Technical Committee Member of MTT-4 on Microwave Passive Components and Transmission Line Structures, MTT-5 on Filters, and MTT-23 on Wireless Communications. He was bestowed by China as the China Overseas Chinese Contribution Award in 2016 and was selected by the IEEE MTT Society as the IEEE Outstanding Young Engineer Award in 2022. He with the Center for ASIS was a recipient of the UESTC Outstanding Team for Teaching and Education Award in 2021 and the UESTC Excellent Team for Postgraduate Supervision Award in 2021. He received the UESTC Outstanding Undergraduate Teaching Promotion Award in 2016 and the UESTC Distinguished Innovation and Teaching Award in 2018. His Research Group BEAM X-Laboratory received multiple best paper awards and best design competition awards, including the IEEE IWS Best Student Paper Award in 2015 and 2018, the IEEE RFIT Best Student Paper Award in 2016 and 2019, the IEEE IMS Best Student Design Competition Award from 2017 to 2019, the IEEE IMS Sixty-Second Presentation Competition Award in 2019, the IEEE RFIC Best Student Paper Award in 2021, and multiple best paper award finalists from the IEEE conferences. He was the TPC Co-Chair of the IEEE IWS in 2018 and the IEEE RFIT in 2019. He is the Vice-Chair of the IEEE MTT-Society Chengdu Chapter. He serves as an Associate Editor for *IET Microwaves, Antennas and Propagation*. He was the Track Editor of IEEE MICROWAVE AND WIRELESS COMPONENTS LETTERS from 2018 to 2021.